Multiscale modeling of the atmospheric environment over a forest canopy

Chao YAN[1,2], Shiguang MIAO[1*], Yujue LIU[1] & Guixiang CUI[3]

[1] *Institute of Urban Meteorology, China Meteorological Administration, Beijing 100089, China;*
[2] *Institute of Atmospheric Physics, Chinese Academy of Sciences, Beijing 100029, China;*
[3] *Department of Engineering Mechanics, Tsinghua University, Beijing 100084, China*

Abstract Vegetation constitutes one of the fundamental types of land use on Earth. The presence of trees in urban areas can decrease local winds and exchange sensible and latent heat with the surrounding environments, thus exerting notable influences on the urban microenvironment. A better understanding of the turbulent transfer of momentum and scalars around vegetation canopy could significantly contribute to improvement of the urban environment. This work develops a large-eddy simulation (LES) method that is applicable to model the flow and scalar transport over the forest canopy. We study the atmospheric flow over complex forested areas under typical weather conditions by coupling LES to the mesoscale model. Models of radiation and energy balance have been developed with explicit treatment of the vegetation canopy. By examining the flow over a forest canopy under a range of stability conditions, we found that buoyancy enhances or suppresses turbulent mixing in unstable or stable atmosphere respectively, with decreasing or increasing wind shear, respectively. From the multiscale modeling of the Beijing Olympic Forest Park, the present coupling scheme proves to better resolve the diurnal variations in wind speed, temperature, and relative humidity over complex urban terrains. The coupling scheme is superior to the traditional mesoscale model in terms of wind field simulation. This is mainly because the coupling scheme not only takes the influences of external mesoscale flow into consideration, but also resolves the heterogeneous urban surface at a fine scale by downscaling, thus better reproducing the complex flow and turbulent transport in the urban roughness sublayer.

Keywords Urban forest environment, Canopy turbulence, Large eddy simulation, Multiscale modeling

1. Introduction

Changes in the urban land cover impact the energy budget of urban canopies and have profoundly influenced the urban environment (Jiang et al., 2010; Arya, 2001), such as the formation of the urban heat island, i.e., the urban area is warmer than the rural community. Urban vegetated areas can significantly decrease the urban impervious surface fraction and increase the rates of evapotranspiration and infiltration of water, which effectively improve the urban micro-

environment, e.g., wind velocity, air temperature and humidity (Bonan, 2016). Therefore, a better understanding of the vegetation-atmosphere interaction and the underlying physical mechanisms of the turbulent transfer of fluxes is of crucial importance for the prediction and improvement of the urban atmospheric environment (Ji and Miao, 1994; Liu et al., 2004).

Vegetation is an important source/sink of scalars such as heat and moisture, the distributions of which inside the canopy depend on the vegetation types (i.e., grass, bushes, and trees) and is difficult to describe accurately. Under fair weather conditions, vegetation absorbs solar radiation and

---

* Corresponding author (email: sgmiao@ium.cn)

exchanges fluxes of momentum and heat with the surrounding environment, thus directly influencing the evolution of turbulent motions in the atmospheric boundary layer (ABL) (Yin, 1991). Nevertheless, most of the previous studies on atmospheric environments over vegetation canopies are carried out under neutral atmospheric conditions, and only a few studies have studied the thermodynamics of vegetation. In terms of in situ observations, Shaw et al. (1988) conducted turbulence measurements within and above a deciduous forest in Ontario, Canada. They found that the canopy drag coefficient was nearly independent of the forest density but decreased greatly with increasing atmospheric stability, and the turbulence transfer became less efficient within the canopy layer as stable stratification increased. Gao et al. (1989) performed measurements of the time series of temperature and humidity fluctuations at different heights at the same experimental site. They concluded that events of ejections and sweeps dominate turbulent transport. Near the top of the forest, the ejecting motion transports warm and moist air out of the forest, while the sweeping motion carries cool and dry air into the canopy. By analyzing the measurements of turbulent statistics in the Amazon rain forest, Kruijt et al. (2000) concluded that rapid downward sweeps became relatively weak due to the concentration of leaf area in the upper canopy, which led to attenuation of the turbulent transfer between the regions inside and outside the canopy. This was mainly because the leaves of the tree canopy absorbed most of the solar radiation resulting in the stable conditions prevailing near the bottom of the canopy layer. Villani et al. (2003) found that the profiles of turbulence statistics were generally invariant with the stability within the canopy based on measurements collected in a broadleaf forest. Launiainen et al. (2007) examined the meteorological quantities in a pine forest at the University of Helsinki across four stability classes. They studied the effects of atmospheric stability conditions on the bulk flow and turbulence statistics. The results showed that the turbulent length scale was suppressed, and the turbulent motions and level of intensity were weakened as the atmospheric stability increased. Su et al. (2008) reached similar conclusions from observations in a broadleaf forest at the University of Michigan that the attenuations of the Reynolds stresses and velocity variances within the canopy layer were more rapid under stable conditions. Wang et al. (2014) investigated the scalar transport of temperature and water vapor using tower-based measurements. Quadrant analysis showed that the transport efficiency of heat was higher than that of water vapor under unstable conditions. Arnqvist et al. (2015) studied the atmospheric flow over a forested site located inland from the Swedish southeastern coast and examined the applicability of the Monin-Obukhov (M-O) theory using measured data from a tall tower. They found that the M-O flux-gradient relations were not applicable within the forest canopy layer

and roughness sublayer because the underlying ground was not homogeneous.

The measurements in field or wind-tunnel experiments are often limited to a finite number of spatial locations and are unable to provide detailed three-dimensional spatial information. With the rapid development of computational resources, using numerical methods to study the flow in complex urban environments has received more attention and has achieved many important results. The commonly used numerical methods fall into three categories: direct numerical simulation (DNS), large-eddy simulation (LES), and Reynolds-averaged Navier-Stokes (RANS) methods. Among these mehtods, LES is an effective method for studying flow in the urban boundary layer and over complex terrains (Li et al., 2015; Liu et al., 2018). LES only resolves large-scale structures and constructs subgrid-scale (SGS) models for small-scale structures of isotropic behavior. LES is able to resolve the fine-scale structure in the boundary layer compared to RANS and can significantly reduce the computational cost compared to DNS (Jiang and Miao, 2004).

Using the LES method, Dwyer et al. (1997), Shen and Leclerc (1997), and Nebenführ and Davidson (2015) examined the budget equation of the turbulent kinetic energy (TKE) for the airflow over a horizontally homogeneous forest canopy in a range of thermal stability classes. Nebenführ and Davidson (2015) found that pressure transport served as the dominant source term of TKE transport inside the canopy under stable conditions. Bohrer et al. (2009) investigated the effects of canopy heterogeneity on forest-atmosphere interactions. It was shown that such microscale heterogeneity directly affected the spatial pattern of ejection-sweep events. Nonetheless, the sensible and latent heat flux exchange between the forest and atmosphere was achieved by specifying the distribution of heat sources within the canopy in their simulations. This simplified model is capable of accounting for the dynamics and thermodynamics of the forested environment, but the assumption that the heat flux is horizontally homogeneous and constant in time may not fully reflect the real circumstances.

Urban environment modeling needs to fully account for the various physical processes that occur within the ABL, especially the effects of vegetation, soil, and buildings on the energy partitioning between sensible and latent heat fluxes (Tjernström, 1989). However, most previous research on the simulation of the atmospheric flow over a vegetation canopy employed idealized boundary and initial conditions, neglecting the impact of synoptic weather conditions on the urban boundary layer (Moeng et al., 2007). Based on the current understanding of canopy turbulence stated above, a multiscale modeling method has been developed here by coupling LES to the mesoscale Weather Research and Forecasting (WRF) model. This method accounts for mul-

tiple atmospheric physical processes over urban vegetation canopies, such as radiation and sensible/latent heat transfer. We use this multiscale model to study the turbulent flow and scalar transport over a three-dimensional heterogeneous canopy, i.e., the Beijing Olympic Forest Park.

2. Large-eddy simulation of forest canopy flow

2.1 Governing equations

The flow and heat transfer over forest canopies follow the basic laws for the conservation of mass, momentum, and energy. We focus on the flow and scalar transport over vegetated regions, and the atmosphere around the forest canopy is treated as an incompressible, Newtonian fluid. The Boussinesq approximation is used here, which only accounts for the density variations associated with the temperature differences. The governing equations are the low-pass-filtered continuity equation, Navier-Stokes (N-S) equation, and the advection-diffusion equations of heat and moisture:

$$\partial \tilde{u}_i / \partial x_i = 0, \tag{1}$$

$$\frac{\partial \tilde{u}_i}{\partial t} + \frac{\partial \tilde{u}_i \tilde{u}_j}{\partial x_j} = -\frac{1}{\rho}\frac{\partial \tilde{p}}{\partial x_i} + \frac{\partial \tau_{ij}}{\partial x_j} + v\frac{\partial^2 \tilde{u}_i}{\partial x_j \partial x_j} + g\frac{\tilde{\theta}}{\theta_0}\delta_{i3} + F_i, \tag{2}$$

$$\frac{\partial \tilde{\theta}}{\partial t} + \frac{\partial\left(\tilde{u}_i \tilde{\theta}\right)}{\partial x_i} = \frac{\partial \tau_{\theta i}}{\partial x_i} + \frac{v}{Pr}\frac{\partial^2 \tilde{\theta}}{\partial x_j \partial x_j} + S_\theta, \tag{3}$$

$$\frac{\partial \tilde{q}}{\partial t} + \frac{\partial(\tilde{u}_i \tilde{q})}{\partial x_i} = \frac{\partial \tau_{qi}}{\partial x_i} + \frac{v}{Sc}\frac{\partial^2 \tilde{q}}{\partial x_j \partial x_j} + S_q. \tag{4}$$

In these equations, the tilde indicates the filtered variables, where $x_i(x_1 = x, x_2 = y, x_3 = z)$ represents the streamwise, lateral, and vertical directions, respectively, $\tilde{u}_i(\tilde{u}_1 = u, \tilde{u}_2 = v, \tilde{u}_3 = w)$ is the filtered velocity component in the x_i direction, ρ (1.208 kg m^{-3}) and v (1.5×10^{-5} m^2 s^{-1}) are the air density and kinematic viscosity, respectively, $\tilde{p}$ is the pressure, $\tilde{\theta}$ is the potential temperature, $\tilde{q}$ is the specific air humidity, g=9.81 m s^{-2} is the gravitational acceleration, δ_{ij} is the Kronecker delta function, and $g\tilde{\theta}\delta_{i3}/\theta_0$ is the buoyancy term, where θ_0 is the reference temperature. F_i represents the drag force term induced by the vegetation canopy, and S_θ and S_q are the source terms of heat and moisture, respectively. The nondimensional parameters Pr and Sc are the molecular Prandtl number and Schmidt number, respectively. The Coriolis force is neglected since we are mainly focused on the flow features in the surface layer. The subgrid-scale (SGS) stress tensor $\tau_{ij} = \tilde{u}_i \tilde{u}_j - \widetilde{u_i u_j}$, heat fluxes $\tau_{\theta i} = \tilde{u}_i \tilde{\theta} - \widetilde{u_i \theta}$, and moisture fluxes $\tau_{qi} = \tilde{u}_i \tilde{q} - \widetilde{u_i q}$, which reflect the effects of the unresolved SGS structures on the resolved larger-scale fluid motions, require SGS parameterizations in terms of the known re-

solved-scale variables for closure of the governing equations.

2.2 Subgrid-scale parameterization of the turbulence

Because large-scale coherent structures, which are caused by shear instability at the canopy interface, dominate the turbulent transfer between the canopy and ambient environment, counter-gradient diffusion of momentum, temperature, and water vapor mixing ratio could occur within the canopy layer (Finnigan et al., 2009). The traditional Smagorinsky model for LES is overly dissipative and fails to account for such backscatter energy transfer (Finnigan, 2000). Thus, the dynamic Lagrangian model proposed in Meneveau et al. (1996) is applied here, i.e., the SGS fluxes are estimated by the following eddy-viscosity model:

$$\tau_{ij} = 2v_t \tilde{S}_{ij} + \tau_{kk}\delta_{ij}/3, \tag{5}$$

$$\tau_{\theta i} = \frac{v_t}{Pr_t}\frac{\partial \tilde{\theta}}{\partial x_i}, \tag{6}$$

$$\tau_{qi} = \frac{v_t}{Sc_t}\frac{\partial \tilde{q}}{\partial x_i}, \tag{7}$$

in which $\tilde{S}_{ij} = \left(\partial \tilde{u}_i / \partial x_j + \partial \tilde{u}_j / \partial x_i\right)/2$ is the strain-rate tensor, Pr_t is the turbulent Prandtl number, Sc_t is the turbulent Schmidt number, v_t is the turbulent eddy viscosity expressed as $v_t = (C_s\Delta)^2\sqrt{2\tilde{S}_{ij}\tilde{S}_{ij}}$, where $\Delta = \sqrt[3]{\Delta x \Delta y \Delta z}$ is the filter scale. The model coefficient C_s is determined dynamically based on the Lagrangian dynamic procedure (Meneveau et al., 1996). In addition to the grid filtering operation, this dynamic procedure involves a second filtering with a filter width twice as large as the grid spacing. The SGS heat fluxes $\tau_{\theta i}$ and moisture fluxes τ_{qi} can be calculated once the eddy viscosity v_t is obtained. The eddy viscosity is averaged over the fluid path lines, which does not increase the computational cost very much. This dynamic model has been widely applied to simulate complex flows over forest canopies and urban environments (Yue et al., 2007; Liu et al., 2011; Li et al., 2018).

2.3 Numerical scheme

The above governing equations are discretized using a cell-centered finite volume method in semi-discrete form, which approximate the integral form of the governing equations in a system of algebraic equations. The variables are defined on a Cartesian mesh in a collocated arrangement. The convective terms are discretized using the Quadratic Upstream Interpolation for Convective Kinetics (QUICK) scheme, while the diffusive terms are discretized using a second-order central difference scheme. The Semi-Implicit Method for Pressure-Linked Equations (SIMPLE) algorithm and momentum interpolation are employed to solve the pressure and

velocity coupling. Time integration is performed by the four-step Runge-Kutta scheme with fourth-order accuracy. Because the finite volume method is conservative, it has been widely applied to study turbulent flow and heat transfer problems (Tao, 2004; Versteeg and Malalasekera, 2007).

2.4　Numerical representation of the forest canopy

Because of the random distribution of leaves and branches, consideration of the detailed canopy morphology remains extremely difficult. Thus, the forest canopy has long been treated as a source or sink of flow resistance and scalars in theoretical analysis and numerical simulations, and its effects are accounted for by adding these source/sink terms to the governing equations. The body force term F_i in eq. (2) is parametrized as the product of the leaf area density (LAD) a (x, y, z), the drag coefficient C_D, and the wind speed as:

$$F_i(x, y, z) = C_D a(x, y, z) U \tilde{u}_i, \qquad (8)$$

in which U is the magnitude of the velocity. This canopy drag model can be applied to different types of vegetation (i.e., grass, bushes, and trees) by varying C_D and $a(x, y, z)$, e.g., using this model, Gillies et al. (2002) measured C_D of fountain grass, burning bush, and spruce in a wind-tunnel experiment; Yue et al. (2007) simulated the atmospheric flow over a corn canopy; Dupont and Brunet (2008) examined the sensitivity of the flow to the morphology of the canopy using LES by varying the leaf area index (LAI) and LAD profile.

Similarly, the source and sink terms, S_θ and S_q, respectively, in the governing equations reflect that the forest foliage absorbs solar radiation and, in turn, warms the surrounding air. Hence, the strengths of S_θ and S_q are proportional to the absorbed shortwave radiation flux and are expressed as the vertical derivatives of the sensible heat flux H and latent heat flux λE, respectively, as:

$$S_\theta(x, y, z) = \frac{1}{\rho c_p} \frac{\partial H(x, y)}{\partial z}, \qquad (9)$$

$$S_q(x, y, z) = \frac{1}{\rho c_v} \frac{\partial [\lambda E(x, y)]}{\partial z}, \qquad (10)$$

in which c_p and c_v are the specific heat capacity of the air at constant pressure and volume, respectively, and λ is the latent heat of vaporization.

The LAD distribution is an important parameter in describing the structure of the forest canopy and is also a key input condition for the numerical modeling of the atmospheric flow over forested environments (Lalic and Mihailovic, 2004). LAD varies with time and space and has a direct impact on the mass, momentum, and energy exchange between the canopy and the atmosphere. However, it is difficult to accurately measure the LAD of a natural forest canopy, and related datasets are also lacking. At present, the methods for obtaining the LAD distribution in numerical simulations include virtual canopy generator (Bohrer et al., 2007, 2009),

laser scanning (Schlegel et al., 2012, 2015), and empirical models (Amorim et al., 2013; Nebenführ and Davidson, 2015). Here, we adopt the empirical relation of LAD inside the forest proposed by Lalic and Mihailovic (2004):

$$a(z) = a_m \left(\frac{h - z_m}{h - z} \right)^n \exp\left[n \left(1 - \frac{h - z_m}{h - z} \right) \right], \qquad (11)$$

where

$$n = \begin{cases} 6, & 0 \le z < z_m, \\ 1/2, & z_m \le z < h, \end{cases} \qquad (12)$$

in which h is the tree height and a_m is the maximum value of LAD at the corresponding height z_m. The LAI, defined as the leaf area per unit ground surface area, can be then calculated by vertically integrating the LAD profile. Lalic and Mihailovic (2004) validated the above relation by comparing the calculated values with measurements from eight observational sites located in four different types of forest (pine, common maple, oak, and silver birch). According to Lalic and Mihailovic (2004), depending on the relative relation between z_m and h, this empirical model can be used to describe the canopy structure for various types of forest communities. For brevity, the tilde symbols used to denote resolved variables are ignored to simplify the notation henceforth.

2.5　Model validation

In this section, we examine the thermodynamic interaction between the forest canopy and ambient atmosphere by modeling the airflow over a horizontally homogeneous canopy under different atmospheric stability conditions using LES. The heat flux distribution within the canopy layer is specified to reflect the solar radiation absorption and longwave radiation of the forest trees. The simulated results are then compared with the tower-based measurements of Arnqvist et al. (2015). The mean height of the trees h is approximately 20 m, the LAI is approximately 4.3, and the canopy drag coefficient is 0.15. Figure 1a shows the LES computational domain, the size of which is 1200 m (x) ×600 m (y)×400 m (z) in the streamwise, lateral, and vertical directions, respectively. The horizontal domain is divided into uniform cells with a grid spacing of 5m, while the mesh uses 16 points to resolve the canopy in the vertical direction and is uniformly stretched above, with total grid numbers of 240 (x) ×120 (y) ×80 (z). The vertical distribution of LAD is shown in Figure 1b. Ideally, in LES modeling of the ABL flow over forest canopy, the computational domain size should be large enough to resolve the energy-containing eddy motions in the ABL, i.e., the domain height should be comparable to the ABL height (~1 km), and the horizontal size should be larger than the ABL height (Bailey and Stoll, 2013). Moreover, the grid resolution should be small enough

to resolve the canopy morphology and turbulent fluctuations in the inertial subrange. However, most previous research utilized a truncated domain to decrease the computation cost, assuming that the large-scale structures in the outer layer have a minor influence on the turbulent motions in the roughness sublayer (Yue et al., 2007; Bailey et al., 2014; Pan et al., 2014). From LES modeling of the canopy turbulence, Bailey and Stoll (2013) found that the statistical properties are relatively insensitive to the domain size when the domain height is larger than 8 times the canopy height. Thus, we also use a truncated domain here, and the domain height (H =400 m) is chosen to be 20 times the forest height (h=20 m) on the grounds of dimensional analysis, see the appendix in Yan et al. (2017).

The nondimensional parameter used to measure the atmospheric stability is h/L, where L is the Obukhov length defined as:

$$L = -\frac{u_*^3 \theta_0}{\kappa g Q_h},$$ (13)

in which u_* is the friction velocity, κ=0.41 is the von Karman constant, and Q_h is the vertical heat flux at the canopy top. The strength of the heat source term S_θ in eq. (3) is proportional to the shortwave solar radiation absorbed by the forest. Assuming that the distribution of the heat flux deceases exponentially (Shaw and Schumann, 1992; Bonan, 2016), S_θ has the following form:

$$S_\theta(z) = \frac{\partial}{\partial z}[Q_h \cdot \exp(-\alpha A_c)],$$ (14)

where α (=0.6) is an extinction coefficient, and A_c is the downward cumulative LAI expressed as:

$$A_c = \int_z^h a(x,y,z)\mathrm{d}z.$$ (15)

Table 1 lists the computational parameters of the LES cases, in which u_* is calculated based on the Reynolds stress at z=2h following the same definition in the field experiment of Arnqvist et al. (2015). By varying the value of Q_h, we examine the effects of different stability classes on the atmospheric flow. A log-law wind profile and a constant-potential temperature (300 K) profile are initially prescribed, with random fluctuations imposed to facilitate the flow transition to a fully developed turbulent state. Since the buoyancy term can enhance or suppress turbulent motions, leading to an increase or decrease, respectively, in the turbulent length scale, the timestep size and spin-up time are also dependent on the atmospheric stability (Launiainen et al., 2007). A constant Courant-Friedrichs-Lewy (CFL) number is used in each simulation, i.e., CFL=0.25 in the unstable cases and CFL=0.02 in the stable cases, to ensure numerical stability. The quantities are averaged over long time intervals (100000 timesteps) after the horizontally averaged wind profile has reached the statistically steady state.

Note that u_* is approximately 0.8 m s^{-1} in the unstable cases, corresponding to a moderate wind condition, which is very common for the flow over a dense forest canopy, see Parlange and Brutsaert (1989) and Nakai et al. (2008). Additionally, increasing u_* properly in numerical simulations enables the flow to reach the equilibrium state faster. This is because in the ABL, the length scale of the energy-containing eddies is approximately the ABL height, z_i~1000 m, and their characteristic time scale (i.e., the eddy turnover
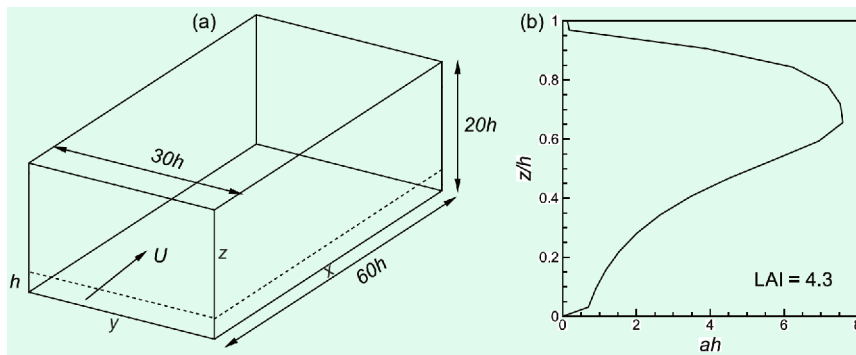

Figure 1 Schematic of LES modeling of the forest canopy flow: (a) three-dimensional computational domain and coordinate system, (b) vertical distribution of LAD.

Table 1 Parameters of the LES runs

Case	Q_h (K m s^{-1})	u_* (m s^{-1})	h/L	Stability classes
1	0.15	0.837	−0.20<h/L<−0.05	Unstable
2	0.05	0.838	−0.05<h/L<−0.02	Slightly unstable
3	0	0.835	|h/L|<0.02	Neutral
4	−0.15	0.828	0.02<h/L<0.05	Slightly stable
5	−0.30	0.746	0.05<h/L<0.20	Stable

time) can be defined as z_i/u_*, and the total time interval required in simulations is generally proportional to the eddy turnover time (Pope, 2000). In cases 4 and 5, $Q_h = -0.15$ and -0.3 K m s^{-1} relate to a heat exchange E_h ($=\rho c_p Q_h$) of approximately -181 and -363 W m^{-2}, respectively, between the forest canopy and the overlying atmosphere, which are not commonly seen in real situations. However, the stability parameter h/L is the only dimensionless parameter that determines the flow characteristics according to the similarity theory (see Garratt, 1992). Hence, although the values of u_* and Q_h deviate from actual conditions, the simulated flows will be similar to the real scenarios if they have the same stability numbers h/L.

Periodic boundary conditions are imposed in the horizontal directions, and the free slip condition is used at the top of the computational domain. An external pressure gradient term dP^*/dx that reflects the influence of mesoscale conditions such as the geostrophic wind (Moeng, 1984; Sauer et al., 2016) is added to the momentum equation to counteract the canopy drag. The wall-friction stress is calculated from the velocity field at the first grid level Δ_z using the Obukhov wall function (Shaw and Schumann, 1992; Stoll and Porté-agel, 2006; Bou-Zeid et al., 2007; Finnigan et al., 2009; Nebenführ and Davidson, 2015) as:

$$\tau_{i3,w} = -\left[\frac{\kappa U_{\text{hor}}}{\ln(\Delta_z/z_0)}\right]^2 \frac{\rho u_i}{U_{\text{hor}}}, \quad i = 1, 2, \tag{16}$$

in which $\tau_{i3,w}$ is the wall stress in the i-th direction, U_{hor} is the mean wind speed at Δ_z, and $z_0 = 0.001h$ is the aerodynamic

roughness length (see Shaw and Schumann, 1992). The bottom wall is assumed to be adiabatic since the LAI is very large and only a small amount of solar radiation will reach the ground through the canopy layer. Because of the use of periodic conditions and the external heat source (or sink) within the canopy layer, the temperature inside the computational domain will continue to increase (or decrease). Thus, a mean temperature gradient term $\delta_{i1}u_i\partial\Theta/\partial x_i$ is added to the temperature convection-diffusion equation to enable the temperature to reach the steady state. Note that in the LES work of Nebenführ and Davidson (2015), they assume that the governing equations are not dependent on the absolute temperature, and the absence of a balance in the temperature equation has a negligible effect on the simulation results.

Figure 2 shows the comparison of the wind profiles between the computed results and the observations of Arnqvist et al. (2015) for the different stability classes. Under unstable conditions, buoyancy enhances turbulent mixing in the atmosphere, and the wind profile above the canopy becomes fuller. Under stable conditions, buoyancy suppresses atmospheric turbulence, and shear production dominates the generation of turbulence so that the wind shear increases as the stability increases. Note that in an unstable ABL, the velocity scale of the energy-containing eddies is the free-convection velocity scale $w_* = \left(gQ_h z_i/\theta_0\right)^{1/3}$. The relationship between w_* and u_* can be expressed as $w_*/u_* = \kappa^{-1/3}\left(-z_i/L\right)^{1/3}$. The use of w_* as the characteristic velocity scale mainly applies to the very unstable ABL with
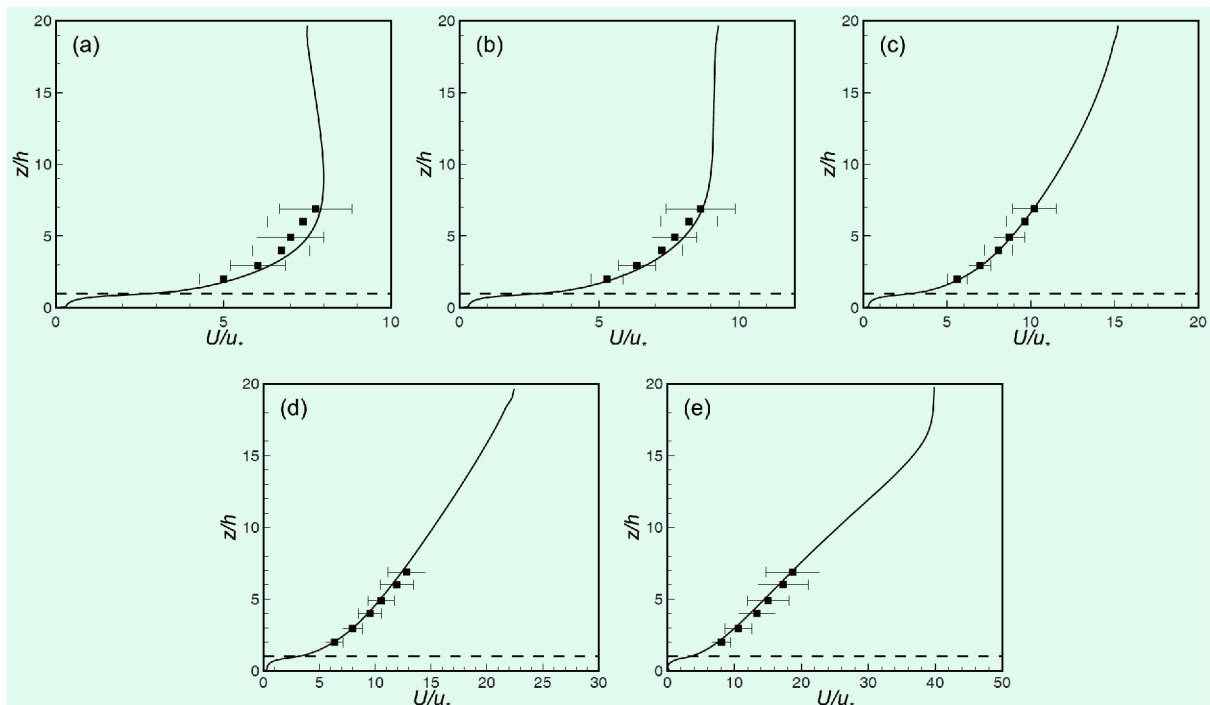

Figure 2 Mean wind speed profiles for the different stability classes. Solid line: LES, symbol and error bar: measurements. (a) Unstable, (b) slightly unstable, (c) neutral, (d) slightly stable, and (e) stable.

zero mean wind (see section 10.4 in Wyngaard, 2010). Here, we focus on the atmospheric stability classes from stable to moderately unstable with $-0.20 < h/L < 0.20$ (Table 1), then $w_* / u_* < 2.9$, i.e., they have the same order of magnitude. Thus, we use u_* as the scaling velocity for all cases.

The vertical distribution of the normalized turbulent momentum flux is shown in Figure 3, from which we can see that the Reynolds stress decreases with the height above the

canopy for all cases. Figure 4 depicts the normalized standard deviations of the streamwise and vertical velocity components, the maximum values of which are $\sigma_u / u_* \approx 2.0$ and $\sigma_w / u_* \approx 1.2$, respectively, for the neutral case, which are consistent with observations in the surface layer (see Wyngaard, 2010). When the atmosphere is stable or slightly stable, the computed results of σ_u are in good agreement with the measured data, while the simulations underestimate the
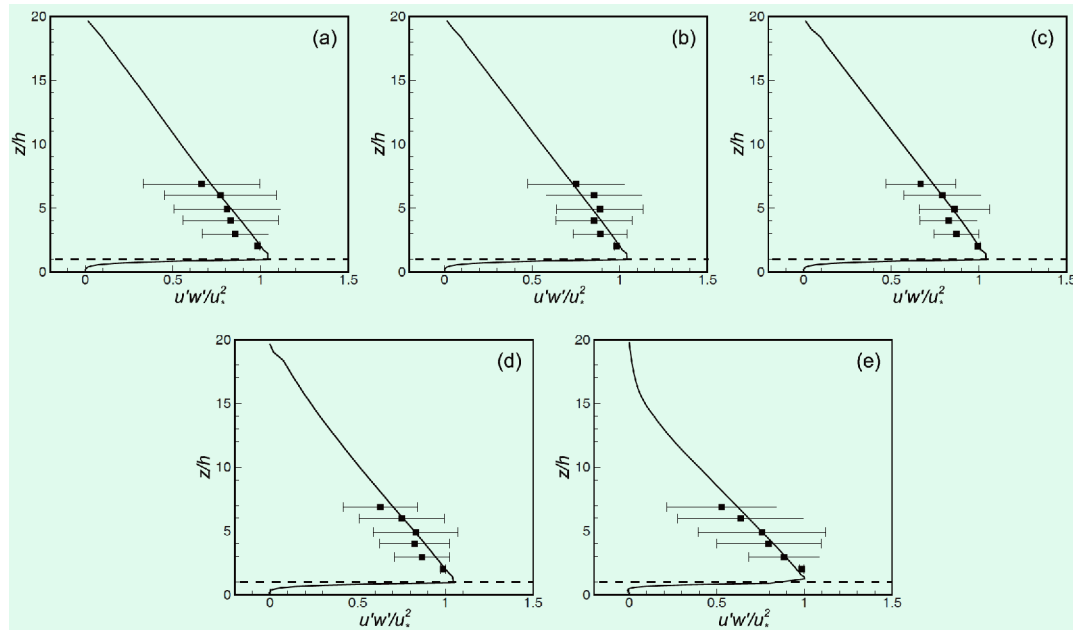

Figure 3   Normalized vertical momentum flux in the streamwise direction for the different stability classes. For the legend, see the caption of Figure 2.
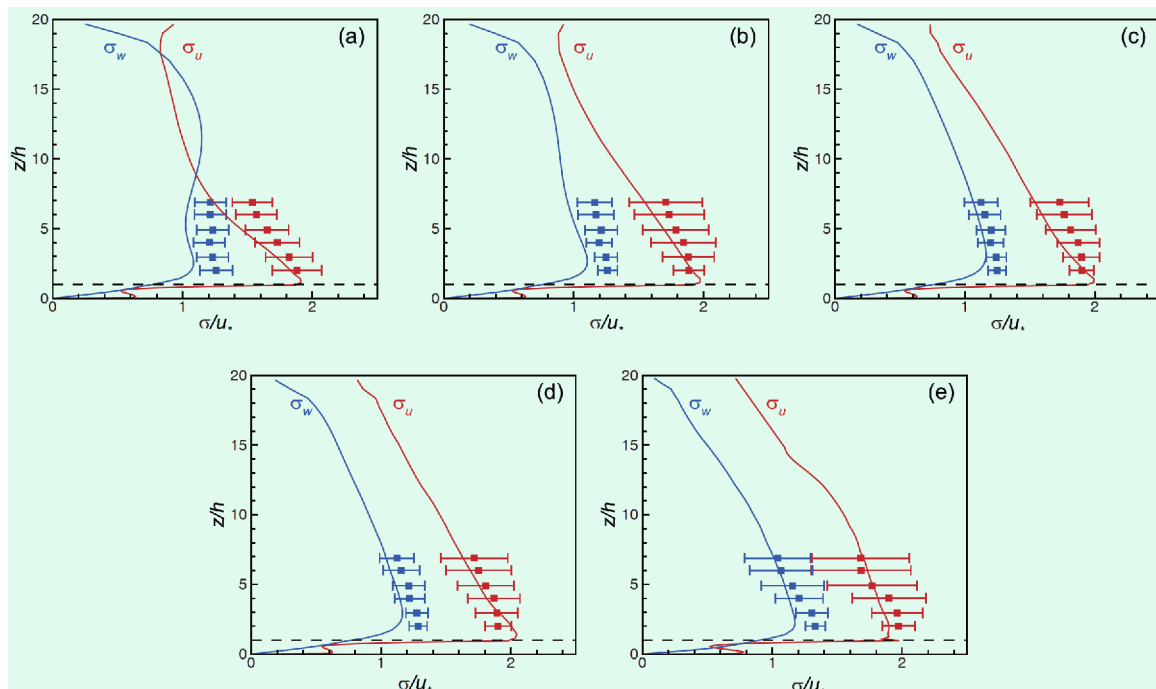

Figure 4   Normalized standard deviations of the streamwise and vertical velocity components for the different stability classes. For the legend, see the caption of Figure 2.

values in the neutral and unstable cases. For all cases, the simulated results of σ_w are lower than the measurements.

Figures 5 and 6 show the vertical profiles of the skewness of the streamwise and vertical velocity components Sk_u and Sk_w, respectively. The measured values of Sk_u are approximately zero for all stability cases. The results of LES agree well with the experimental data under slightly stable and

stable conditions and deviate from the measurements for the neutral and unstable cases. Similarly, the simulated results of Sk_w agree with the measurements under neutral, slightly stable, and stable conditions but exhibit discrepancies from $z=4h$ to $z=7h$ in the slightly unstable and stable cases. This may be caused by the top boundary condition as the ABL height grows higher under unstable atmosphere conditions.
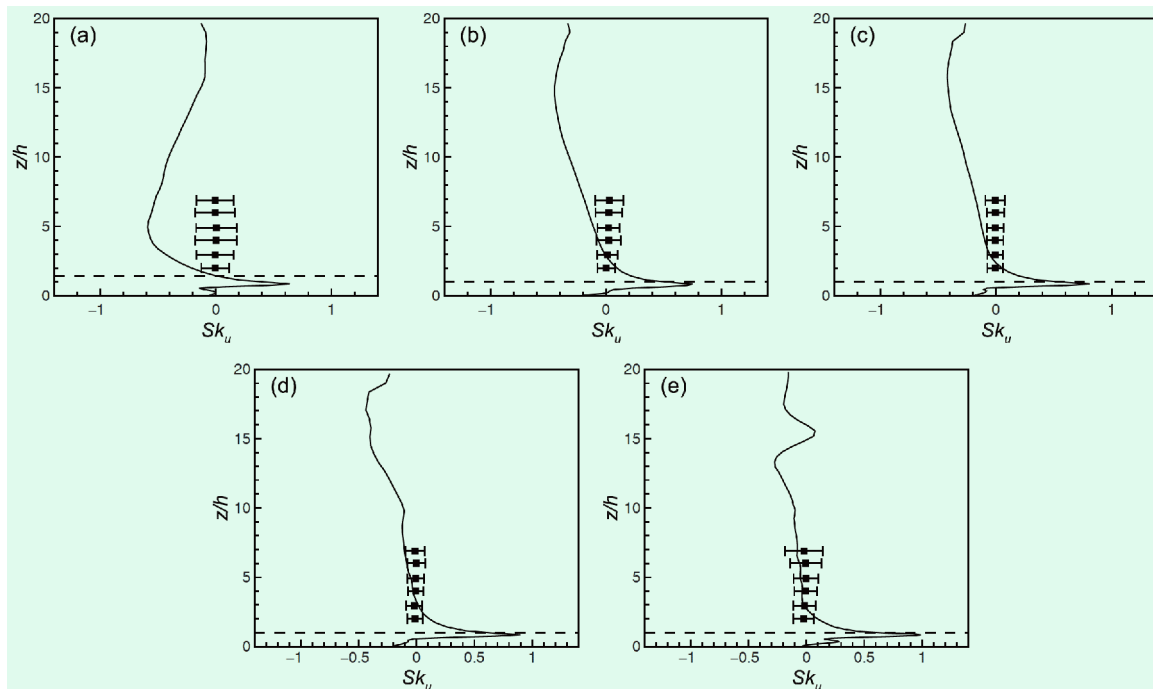

Figure 5   Skewness of the streamwise velocity component for the different stability classes. For the legend, see the caption of Figure 2.
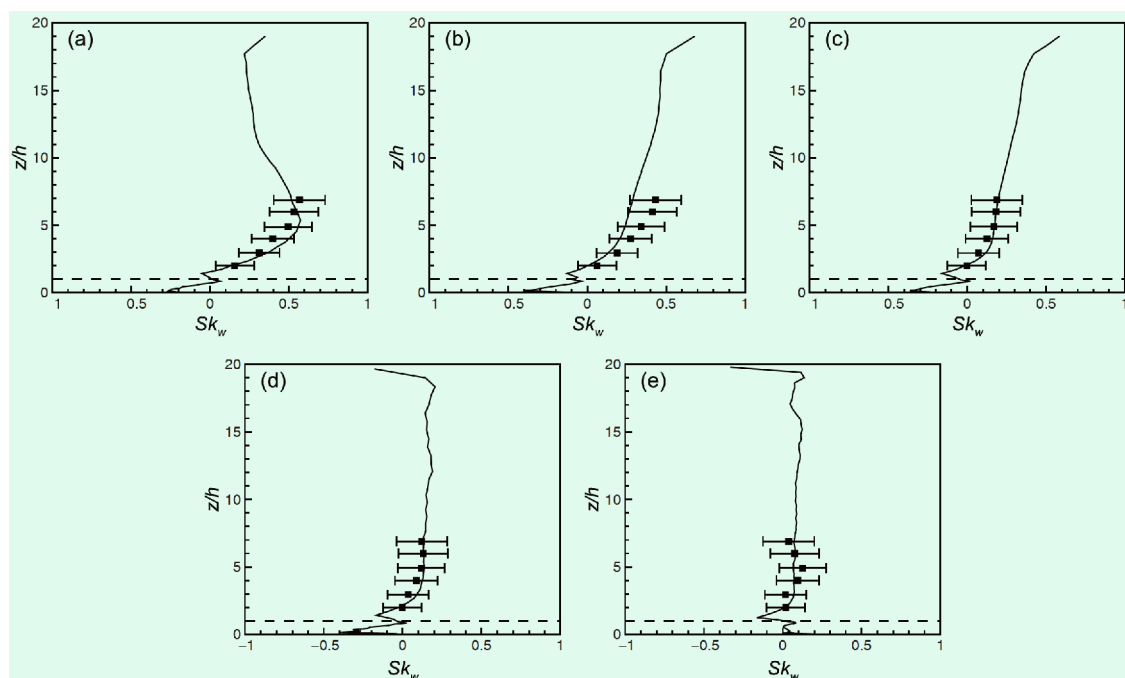

Figure 6   Skewness of the vertical velocity component for the different stability classes. For the legend, see the caption of Figure 2.

Overall, the simulated statistics show a good agreement with the observations, which indicates that the empirical relation of the LAI and the numerical method used here are well suited for modeling atmospheric flow under different atmospheric stability conditions.

3.   Multiscale modeling of the atmospheric flow over the Beijing Olympic Forest Park

The urban green space is composed of various land cover types that are inhomogeneous in the horizontal direction. Thus, the use of idealistic initial and boundary conditions makes it very difficult to simulate realistic flows (Moeng et al., 2007). Therefore, we couple the aforementioned LES method to the mesoscale model WRF and simulate the microscale atmospheric environment over the Olympic Forest Park, aimed at studying the spatial-temporal variations in meteorological fields such as wind, temperature, and humidity over urban vegetated areas.

3.1   Simulation set-up

The Olympic Forest Park (40.25°N, 116.39°E) is situated on the northern end of the central axis of Beijing, which was built for the Beijing 2008 Olympic Games. The park also increases the urban greenspace and improves the air quality. It is divided by the North Fifth Ring Road into a Northern Garden and a Southern Garden, with a total area of 6.8 square kilometers. The green space covered an area of 4.8 square kilometers, and the green coverage rate reached 95.6%. There are 55 million trees and shrubs and approximately 280 species of plant, composed mainly of broadleaf deciduous and evergreen coniferous trees.

The computational domain of LES is centered at the Olympic Forest Park and starts from Xueqing Road and ends at Beiyuan Road from west to east and extends from Kehui Road to Hongjunying South Road from south to north. The domain size is 5.4 km in the east-west direction and 2.5 km in the north-south direction, with a vertical height of 1 km. A terrain-following coordinate system is used for the complex terrain area, and the immersed boundary method is employed to resolve the buildings in the Forest Park. A schematic of the computational domain and associated mesh design is shown in Figure 7. The coordinates will be transformed to be parallel to the gently undulating topography using the Jacobian matrix in the simulations. The white circle in Figure 7b is the location of the automatic weather station (AWS, 40.02°N, 116.39°E) in the park, from which the measured data are used to compare the results between the simulations and observations. A combined model for the urban canopy is used to decrease the computational cost (Liu et al., 2012), i.e., the shape of the buildings and LAD distributions are resolved in fine grids of 5 m horizontal resolution in the central area of the domain, while coarse grids of 45 m spacing are used outside, and the buildings are treated with a drag force f_i expressed as:

$$f_i(x, y, z) = U u_i / L_c, \tag{17}$$

in which L_c is the canopy-drag length scale that is inversely proportional to the canopy drag coefficient and roughness density as proposed in Belcher et al. (2003):

$$L_c = \frac{2(1 - \phi) h_c}{\bar{c}_d \lambda}, \tag{18}$$

in which $\bar{c}_d = 3.0$ is the average drag coefficient. The volume fraction of buildings ϕ, the roughness height h_c, and the roughness density λ are all functions of the spatial coordinates.

The distributions of the canopy height and LAI are two important factors that affect the transfer of radiation inside
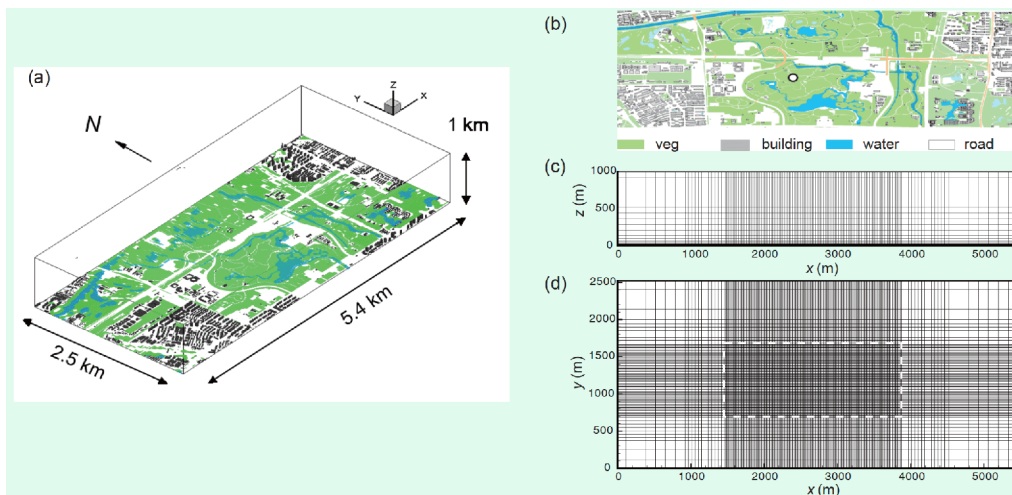

Figure 7   Schematic of the flow over the Olympic Forest Park: (a) the distribution of the land cover, (b) the different types of surface cover, (c) the grid distribution in an *x-z* slice, (d) the grid distribution in an *x-y* slice.

the canopy and determine the forest-atmosphere interaction (Xu et al., 2014). Here, the mean canopy height is assumed to be 20 m because of the paucity of reliable data. For the LAI, Liu et al. (2015) estimated the seasonal variations in the LAI in mixed evergreen-deciduous forests using the litterfall collection method. By referring to their observed data, the mean LAI is assumed to be 1.49 here. Using a random generation algorithm, the horizontal distributions of LAI and canopy height in the Olympic Forest Park are shown in Figure 8. There are 20 grid points within a distance of 30 m above the ground to fully describe the LAD variation of the forest canopy and resolve the physical processes occurring inside the canopy. The mesh is stretched above with a total grid number of 366×262×50.

3.2   WRF-LES coupling

The WRF model is an open-source model for applications such as numerical weather prediction and simulation of geophysical flows. It is developed by the National Center for Atmospheric Research (NCAR), the National Centers for Environmental Prediction (NCEP), and several other agen-

cies in the United States. The WRF system contains two dynamic solvers, i.e., the Advanced Research WRF (ARW) and Nonhydrostatic Mesoscale Model (NMM), which can be used to simulate events from the synoptic scale to the city scale by grid nesting.

The atmospheric flow over the Olympic Forest Park and surrounding area is modeled using the Advanced Research WRF model version 3.8 with five nested domains (D1–D5, Figure 9). The simulated period starts on December 16, 2015, a typical sunny day in the winter season. Domains 4 and 5 use the LES mode of WRF to capture more detailed city-scale turbulent structures that serve as more reasonable boundary conditions for the present microscale LES model. As shown in Table 2, the horizontal resolutions (grid numbers) for each domain are 12.15 km (91×82), 4.05 km (91×82), 1.35 km (91×82), 0.45 km (91×82), and 0.15 km (100×100). As shown in Figure 9a, the outermost domain D1 covers most parts of the North China Plain, while the innermost domain D5 is centered at the Olympic Forest Park with an area of approximately 15 km×15 km. The vertical direction contains 80 grid points with 26 levels within a distance of 1km above the ground.
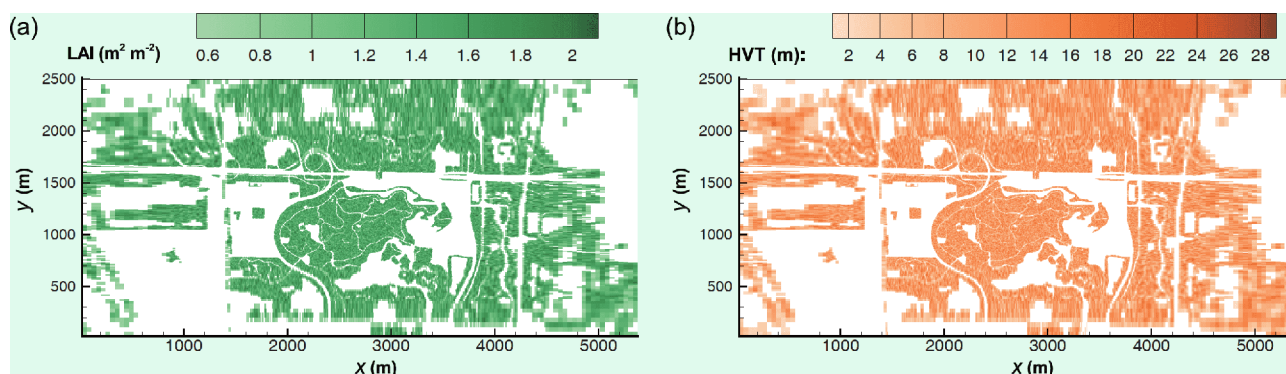

Figure 8   The horizontal distributions of (a) LAI and (b) canopy height in the Olympic Forest Park.
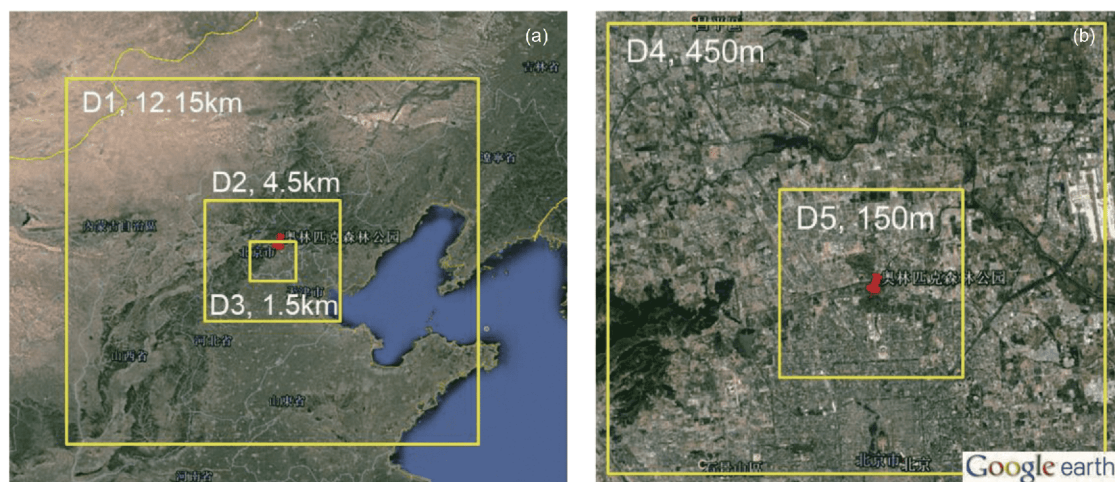

Figure 9   The five nested domains in the mesoscale WRF model: (a) mesoscale simulation domains D1–D3, (b) LES-mode domains D4–D5.

Table 2 The five nested models used for the multiscale simulations

Domain	PBL treatment	Radiation scheme	LSM	Horizontal resolution (km)	Grid points	Time step (s)
D1	YSU	Dudhia+RRTM	Noah	12.15	91×82×80	72
D2	YSU	Dudhia+RRTM	Noah	4.05	91×82×80	24
D3	YSU	Dudhia+RRTM	Noah	1.35	91×82×80	8
D4	LES	Dudhia+RRTM	Noah	0.45	91×82×80	4/3
D5	LES	Dudhia+RRTM	Noah+UCM	0.15	100×100×80	2/9

The initial and boundary conditions for the outermost domain of WRF are obtained from the NCEP operational global final (FNL) analyses on a 1°×1° grid. The field from the parent domain is interpolated to provide the lateral boundary conditions for the child domain. The atmospheric options used in the WRF simulation include the Yonsei University (YSU) planetary boundary layer (PBL) scheme, the Dudhia scheme for shortwave radiation, the Rapid Radiative Transfer Model (RRTM) for longwave radiation, and the Noah land surface scheme for the surface fluxes and temperature. A single-layer urban canopy model (UCM) is also used to solve the energy balance equation in the urban areas. The meteorological field from the innermost domain of WRF is used to provide the initial and time-varying lateral boundary conditions for the present LES domain to reflect the influence of mesoscale meteorological conditions on the microscale environment (Cui et al., 2013; Castro et al., 2015; Barcons et al., 2018).

3.3 Boundary conditions for LES

3.3.1 Lateral and top boundaries

To reproduce the evolution of the environmental flow over vegetated regions, the boundary conditions for the microscale LES experiments are generated by the WRF model using trilinear interpolation in space and linear interpolation in time between two consecutive (15 min apart) WRF files (Castro et al., 2015). The vertical profile of the observed data at the location of the AWS is shown in Figure 10. Since the height of the first layer in WRF is much larger than that in the microscale LES, the boundary values of ϕ (u, v, w, T, q_v) in LES below the first layer of WRF are obtained using power-law interpolation:

$$\frac{\phi - \phi_s}{\phi_{WRF} - \phi_s} = \left(\frac{z}{Z_{WRF}}\right)^{0.27}, z < Z_{WRF}, \tag{19}$$

in which ϕ_s is the surface value of ϕ, and ϕ_{WRF} is the value of ϕ at the first grid point of WRF Z_{WRF}.

3.3.2 Land-surface energy budget

The surface temperature of plants, buildings, and the underlying ground are estimated according to the energy bud-

get. The ground surface temperature T_s and moisture q_s over a diurnal cycle (in seconds) τ are determined by solving the following heat conduction equations:

$$\frac{\partial T_s}{\partial t} = C_T \left(R_{ns} - H_s - \lambda E\right) - \frac{2\pi}{\tau}(T_s - T_{ds}), \tag{20}$$

$$\frac{\partial T_{ds}}{\partial t} = \frac{1}{\tau}(T_s - T_{ds}), \tag{21}$$

in which T_{ds} is the deep ground temperature and C_T is the land surface heat capacity. The net radiative flux R_{ns} in eq. (20) has different forms for different land cover types, i.e., for urban roads and building surfaces, R_{ns} includes the shortwave radiation and the longwave radiation of the air and plants absorbed by the ground surface, as well as the longwave radiation of the ground (Tjernström, 1989):

$$R_{ns} = R_{sw}(1 - \alpha_s) + \sigma\left(\varepsilon_a T_a^4 - \varepsilon_s T_s^4\right) - \varepsilon_s \sigma T_s^4 + \varepsilon_v \sigma T_v^4. \tag{22}$$

For the soil and vegetation-covered parts, the net radiative flux within the canopy layer R_{nv} is composed of the solar shortwave radiation and longwave radiation from the air, vegetation, and ground surface. The shortwave radiation is dependent on LAI and shows an exponential decay (Arya, 2001):

$$R_{nv} = R_{sw}(1 - \alpha_v) \cdot e^{-\alpha A_c} - \varepsilon_v \sigma T_v^4 + \varepsilon_a \sigma T_a^4 + \sigma_v \sigma \varepsilon_s T_s^4, \tag{23}$$

in which α and A_c are the extinction coefficient and downward cumulative LAI, respectively, defined in eq. (15), α_v is the shielding parameter related to vegetation, α_s is the albedo, $\sigma=5.67\times10^{-8}$ W m^{-2} K^{-4} is the Stephan-Boltzmann constant, and $\varepsilon_s (T_s)$, $\varepsilon_a (T_a)$, and $\varepsilon_v (T_v)$ are the emissivity (temperature) of the soil surface, air, and vegetation, respectively. The shortwave radiation R_{sw} is determined from:

$$R_{sw} = S_0 \cos\gamma, \tag{24}$$

in which S$_0$=1368 W m^{-2} is the solar constant and γ is the solar zenith angle defined as:

$$\cos\gamma = \sin\varphi\sin\delta + \cos\varphi\cos\delta\cos h_r, \tag{25}$$

where φ is the latitude, δ is the solar declination, and h_r is the solar hour angle. The sensible heat flux H and latent heat flux λE are estimated from:

$$H_s = \rho c_p C_{hs} U_a (T_s - T_a), \tag{26}$$

$$\lambda E_s = \lambda (E_s + E_{tr}), \tag{27}$$

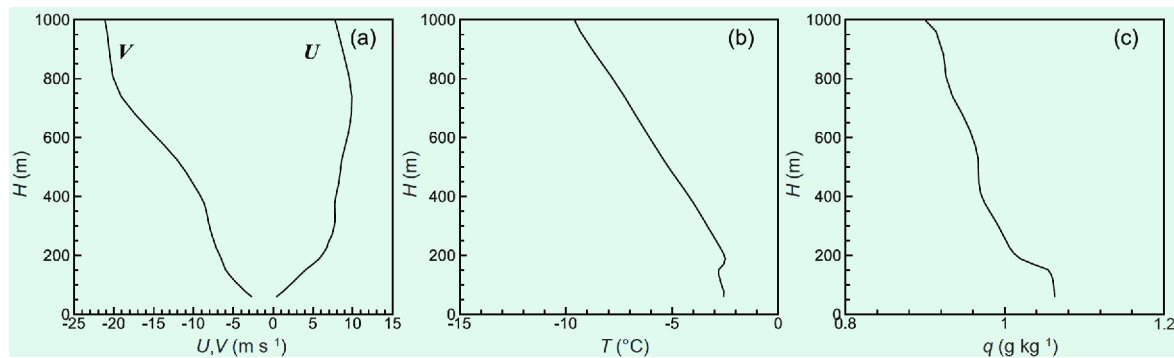in which E_s is the evaporation from the soil surface, and E_{tr} is

Figure 10   The vertical profiles of the WRF-simulated results at the location of the AWS in the Olympic Forest Park on December 16, 2015: (a) wind speed (U, V), (b) air temperature, (c) specific humidity.

the transpiration from plants, defined as:

$$E_s = (1 - f_v)\rho C_{qs} U_a [h_u q_{sat}(T_s) - q_a], \tag{28}$$

$$E_{tr} = f_v \rho C_{ds} U_a [q_{sat}(T_s) - q_a], \tag{29}$$

in which f_v is the fractional coverage of vegetation, C_{hs} and C_{qs} are the exchange coefficients of heat and moisture, respectively, at the soil surface, U_a is the wind speed at the atmospheric level, h_u is the relative humidity at the ground surface depending on the soil surface moisture, and $q_{sat}(T_s)$ is the saturation mixing ratio when the ground surface temperature is T_s.

3.4   Results and discussion

3.4.1   *Diurnal variation of the micrometeorological parameters*

Figure 11 shows the comparisons of the diurnal variations of the 10-m wind speed, 2-m air temperature and relative humidity at the location of the AWS between the results from WRF-LES and observations on December 16, 2015. We can see that the multiscale WRF-LES coupling method developed here is superior to the mesoscale WRF model in simulating the wind speed, and the discrepancies are within an acceptable range. The possible reasons that WRF yields higher wind speeds are twofold:

(1) There is an inherent error associated with the method of calculating the 10-m wind speed in WRF. The WRF model calculates the wind at 10m based on the M-O similarity theory by extrapolating the wind from the first model level (Jiménez et al., 2012). However, the M-O similarity theory is not valid in the urban roughness sublayer (Kaimal and Finnigan, 1994; Foken, 2006). Moreover, the WRF model does not explicitly account for the resistance of the vegetation to the airflow, which results in a higher WRF-simulated wind. Aumond et al. (2013) added the drag force due to trees in the Meso-NH model, and the results confirmed that this drag force approach was more efficient than the roughness approach in describing the canopy flow, especially under stable

and neutral conditions.

(2) Another reason could be the insufficient resolution of the underlying topography. The WRF model used here employs the United States Geological Survey (USGS) 24 categories of land use data with a spatial resolution of 30″ (approximately 1 km×1 km). Although the horizontal resolution of the innermost domain is 150 m, this does not improve the resolution of the topography. This implies that the topographical input data of WRF is smoother than that in the real situation, which may cause WRF to underestimate the resistance of the underlying surface, leading in turn to a higher WRF-simulated wind speed. The simulation of the near-surface wind speed and other weather processes can be improved by introducing a parametric scheme to represent the subgrid-scale topography effects in the numerical weather prediction models (Jiménez and Dudhia, 2012; Lorente-Plazas et al., 2016; Zhou et al., 2017).

In fact, the WRF model usually overestimates the near-surface wind speed (Cheng and Steenburgh, 2005); other factors that cause errors in WRF simulations include the influences of the initial and boundary conditions, as well as simulation errors associated with the weather-scale processes that are beyond the scope of this paper (see Jiménez et al., 2013 for details).

The present LES module incorporates the numerical representation of the forest canopy and employs high-resolution geographic data of the Beijing Olympic Forest Park and its surrounding areas, which mitigates the influences of the causes of error mentioned above and significantly improves the simulation of the wind flow. Note that the WRF-LES simulated wind is comparable to the observation, but quantitatively, there are still certain differences that could be caused by the following two reasons:

(1) The leaves and branches are randomly distributed and may bend due to the wind (Vogel, 1989), which makes it very difficult to obtain accurate information on the LAD in the Beijing Olympic Forest Park. WRF-LES modeling uses a random algorithm and empirical relation to generate the
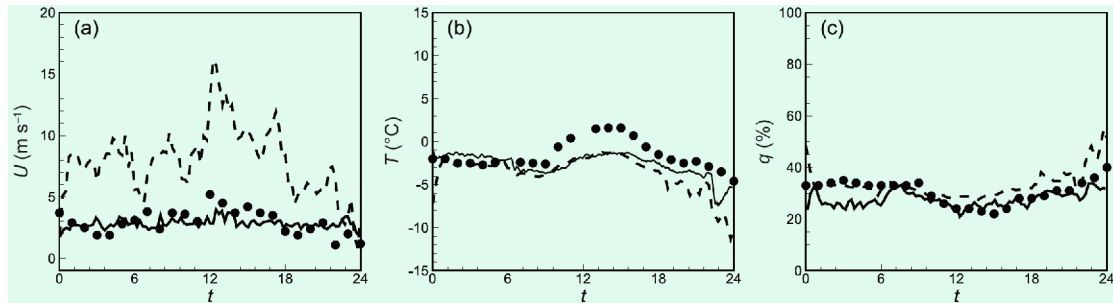
Figure 11   Comparisons of the WRF-LES results and observations. Solid line: WRF-LES results; dashed line: WRF results; symbol: observations. (a) 10-m wind speed, (b) 2-m air temperature, (c) 2-m specific humidity.

three-dimensional spatial distribution of LAD, which is different from that in the real situation. Thus, the microscale canopy heterogeneity is not fully captured, which causes certain errors in the simulation of the wind speed (Bohrer et al., 2009; Schlegel et al., 2012, 2015).

(2) The parametric model of the forest canopy drag (eq. (9)) uses a constant canopy drag coefficient that is uniform in the canopy layer. This model reflects the bulk effect of trees on the airflow, but it may cause errors when applied to the simulation of unsteady flow. Yue et al. (2007) considered the influences of trunks and branches in their LES study, in which the crown parts still used the model with a constant drag coefficient, while the trunk parts used the drag model for circular cylinders. The computation results indicated that the statistics yielded from this model showed a better agreement with measurements. In real situations, the canopy drag coefficient varies with the local wind speed and atmospheric stability (Shaw et al., 1988; Poggi et al., 2004). However, since it is very difficult to derive a theoretical or empirical model for the canopy drag (Pan et al., 2016), a mean drag coefficient is usually used by averaging measurements of the instantaneous velocity over time and with height (Pinard and Wilson, 2001). Hence, this model with a constant drag coefficient has been widely used in numerical simulations of flow over forest canopies (Shaw and Schumann, 1992; Finnigan et al., 2009; Nebenführ and Davidson, 2015).

Both the measured data and computed results plotted in Figure 11b show that the region exhibits a continuous low temperature with an average temperature of approximately −3°C on December 16, 2015. From 13:00 pm to 14:00 pm, the air temperature reaches the highest value of the day. The simulation results of the relative humidity are consistent with the observations, with a value of approximately 30% throughout the day (Figure 11c).

3.4.2   Analysis of the wind field and air temperature field
Given the comparisons shown above, we further examine the distribution and characteristics of the wind and air temperature fields in the Olympic Forest Park. Specifically, the

30-min-averaged physical fields obtained from the multi-scale WRF-LES at 14:00 pm and 20:00 pm are selected for detailed analysis. Figures 12 and 13 show the wind field and temperature field, respectively, at 14:00 pm and 20:00 pm. The *x-z* slice in the figures is located at *y*=1270 m of the LES domain, corresponding to the North Fifth Ring Road; the *y-z* slice is situated at *x*=2700 m of the domain, while the Olympic Forest Park extends from *x*≈1300 to 4200 m. The intensity of solar radiation and sunshine duration become notably smaller and shorter in the winter season. The turbulent motions in the ABL are dominated by the mechanical turbulence generated by wind shear, while the thermal turbulence caused by buoyancy is relatively weaker. Consequently, the vertical gradient of the wind speed increases at a maximum wind speed of 20 m s^{-1} at high altitudes. At 14:00 pm, the ground surface temperature reaches the maximum value −1°C of the day, and the atmosphere is in a slightly unstable state, which to a certain extent enhances the vertical convection. Figure 12a shows that in the *x-z* slice from west to east, a curved streamline forms, and a large-scale circulation (*x*=1600–2200 m) appears at the west boundary of the Olympic Forest Park (*x*≈1850 m). The vertical convection enhances the exchange of heat flux between the urban canopy and overlying atmosphere, and the temperature distribution in the corresponding area is less uniform than that in the downstream area (Figure 12b). Note that the WRF model only provides three-dimensional initial conditions for the LES domain at the beginning of the simulation (0:00 am on December 16, 2015), and thereafter, only the boundary conditions for LES are updated every 15 min by interpolation of the WRF output. The initial condition has a very weak influence on the wind field at 14:00 pm, and this circulation was not found in the initial wind field (not shown). Thus, the large-scale circulation displayed at 14:00 pm may be caused by the interaction between the dynamics and thermodynamics near the forest edge. As the surface type transitions from urban flat ground to forest canopy, this change in land cover may lead to two outcomes: (1) the wind speed deceases rapidly in the forest canopy layer and increases above, forming a circulation structure because of the shear in-

stability (Eder et al., 2013; Pan et al., 2016). As the wind reaches the quasi-equilibrium state in the downwind direction, the wind speed gradient decreases, and the streamlines are no longer curved. (2) At 14:00 pm, the forest canopy and the urban ground absorb solar shortwave radiation and exchange heat with the ambient atmosphere, which contributes to the formation of a circulation structure. Moreover, because the energy budget of the forest canopy is different from that of the urban ground, there is also heat exchange near the forest edge in the horizontal direction, which further boosts the mean flow. At 20:00 pm, due to the longwave radiation that releases heat, the ground surface temperature drops to approximately −4°C. The ABL is in the stable stratification regime, under which vertical motions are suppressed and streamlines are parallel and flat. The temperature decreases monotonically from the ground to the upper atmosphere, with a reduction of approximately 6°C over 1000 m in altitude (Figure 13).

4. Conclusion

In this study, a LES method for modeling the microenvironment over a forest canopy was developed within the framework of finite volume discretization. We examined the effects of temperature stratification on the canopy flow under different atmospheric stability conditions. The simulations showed satisfactory agreements with experimental measurements, lending confidence to the numerical model and representation of the vegetation canopy used here. Buoyancy was found to enhance or suppress turbulent mixing in unstable or stable atmosphere, respectively.

Then, a coupling scheme of WRF-LES was developed and evaluated by modeling the atmospheric flow over the Beijing Olympic Forest Park on a clear day in winter. The output from the WRF model was used to produce time-varying boundary conditions of wind, temperature, and moisture for LES. The sensible and latent heat exchange between the forest canopy and the overlying atmosphere were accounted for using the energy budget equation, thus reflecting the characteristics of momentum and scalar transport over urban vegetated areas in real situations. In comparison to the measurements from an automatic weather station, the multiscale coupling scheme of WRF-LES and mesoscale model WRF produced a similar performance of the temperature and relative humidity that were in good agreement with the observations, but WRF-LES improved the simulation of the wind field compared to the traditional WRF mode, which was mainly because the coupling scheme was capable of better resolving the roughness elements on the ground (vegetation, buildings, etc.) and capturing nonuniform flow fields and flow structures. Through flow visualization of the
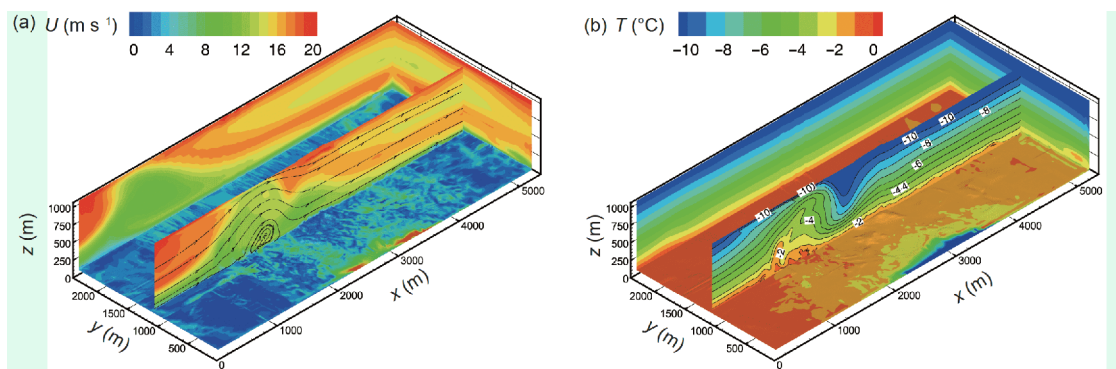

Figure 12   The LES results at 14:00 pm on December 16, 2015: (a) wind field, (2) temperature field.
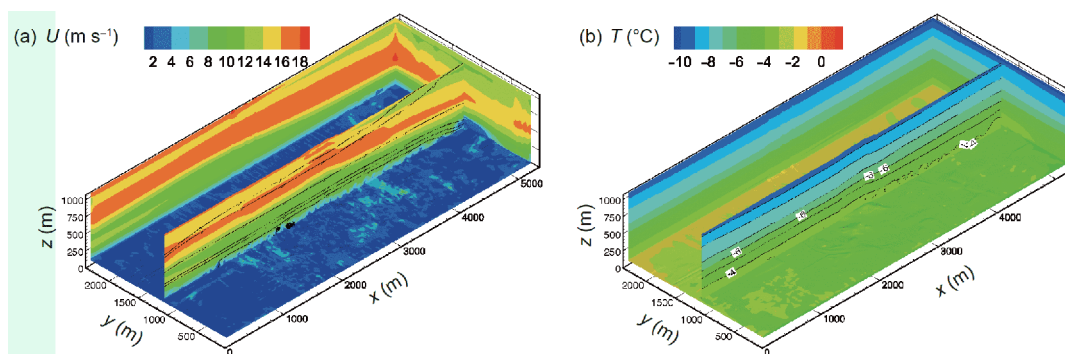

Figure 13   The LES results at 20:00 pm on December 16, 2015: (a) wind field, (2) temperature field.

three-dimensional wind field and temperature over the Beijing Olympic Forest Park, it was found that, by virtue of the high resolution of the fine-scale microscale LES method, WRF-LES reproduced the diurnal variation in micrometeorological parameters and captured the interaction between atmospheric stability and atmospheric flow. In the real-case simulations, the vertical convection was enhanced and a large-scale circulation formed when the atmosphere was slightly unstable, providing positive feedback on the heat exchange between the urban canopy and overlying atmosphere.

Note that only one-way coupling between WRF and LES was developed here, i.e., WRF and LES were run in the offline mode rather than via inline two-way coupling. Following the same methodology, research directions that could be carried out in the future include: (1) using laser scanning to acquire accurate vegetation data, such as LAI and canopy height, and allowing for more realistic modeling of the microenvironment over vegetated areas; (2) flow and scalar transport over complex terrains, such as hills and urban areas with a mosaic of buildings and vegetation; and (3) wind-energy assessment and wind farm micrositing optimization (Breton et al., 2017; Nebenführ and Davidson, 2017).

References

Amorim J H, Rodrigues V, Tavares R, Valente J, Borrego C. 2013. CFD modelling of the aerodynamic effect of trees on urban air pollution dispersion. Sci Total Environ, 461–462: 541–551

Arnqvist J, Segalini A, Dellwik E, Bergström H. 2015. Wind statistics from a forested landscape. Bound-Layer Meteorol, 156: 53–71

Arya S P. 2001. Introduction to Micrometeorology. 2nd ed. California: Academic Press. 420

Aumond P, Masson V, Lac C, Gauvreau B, Dupont S, Berengier M. 2013. Including the drag effects of canopies: Real case large-eddy simulation studies. Bound-Layer Meteorol, 146: 65–80

Bailey B N, Stoll R. 2013. Turbulence in sparse, organized vegetative canopies: A large-eddy simulation study. Bound-Layer Meteorol, 147: 369–400

Bailey B N, Stoll R, Pardyjak E R, Mahaffee W F. 2014. Effect of vegetative canopy architecture on vertical transport of massless particles. Atmos Environ, 95: 480–489

Barcons J, Avila M, Folch A. 2018. A wind field downscaling strategy based on domain segmentation and transfer functions. Wind Energy, 21: 409–425

Belcher S E, Jerram N, Hunt J C R. 2003. Adjustment of a turbulent boundary layer to a canopy of roughness elements. J Fluid Mech, 488: 369–398

Bohrer G, Katul G G, Walko R L, Avissar R. 2009. Exploring the effects of microscale structural heterogeneity of forest canopies using large-eddy simulations. Bound-Layer Meteorol, 132: 351–382

Bohrer G, Wolosin M, Brady R, Avissar R. 2007. A virtual canopy generator (V-CaGe) for modelling complex heterogeneous forest canopies at high resolution. Tellus B-Chem Phys Meteorol, 59: 566–576

Bonan G B. 2016. Ecological Climatology. 3rd ed. Cambridge: Cambridge

University Press. 692

Bou-Zeid E, Parlange M B, Meneveau C. 2007. On the parameterization of surface roughness at regional scales. J Atmos Sci, 64: 216–227

Breton S P, Sumner J, Sørensen J N, Hansen K S, Sarmast S, Ivanell S. 2017. A survey of modelling methods for high-fidelity wind farm simulations using large eddy simulation. Phil Trans R Soc A, 375: 20160097

Castro F A, Silva Santos C, Lopes da Costa J C. 2015. One-way mesoscale-microscale coupling for the simulation of atmospheric flows over complex terrain. Wind Energ, 18: 1251–1272

Cheng W Y Y, Steenburgh W J. 2005. Evaluation of surface sensible weather forecasts by the WRF and the eta models over the western United States. Weather Forecast, 20: 812–821

Cui G X, Zhang Z S, Xu C X, Huang W X. 2013. Research advances in large eddy simulation of urban atmospheric environment (in Chinese). Adv Mech, 43: 295–328

Dupont S, Brunet Y. 2008. Influence of foliar density profile on canopy flow: A large-eddy simulation study. Agric For Meteorol, 148: 976–990

Dwyer M J, Patton E G, Shaw R H. 1997. Turbulent kinetic energy budgets from a large-eddy simulation of airflow above and within a forest canopy. Bound-Layer Meteorol, 84: 23–43

Eder F, Serafimovich A, Foken T. 2013. Coherent structures at a forest edge: Properties, coupling and impact of secondary circulations. Bound-Layer Meteorol, 148: 285–308

Finnigan J. 2000. Turbulence in plant canopies. Annu Rev Fluid Mech, 32: 519–571

Finnigan J J, Shaw R H, Patton E G. 2009. Turbulence structure above a vegetation canopy. J Fluid Mech, 637: 387–424

Foken T. 2006. 50 years of the Monin-Obukhov similarity theory. Bound-Layer Meteorol, 119: 431–447

Gao W, Shaw R H, Paw U K T. 1989. Observation of organized structure in turbulent flow within and above a forest canopy. Bound-Layer Meteorol, 47: 349–377

Garratt J R. 1992. The Atmospheric Boundary Layer. Cambridge: Cambridge University Press. 316

Gillies J A, Nickling W G, King J. 2002. Drag coefficient and plant form response to wind speed in three plant species: Burning Bush (*Euonymus alatus*), Colorado Blue Spruce (*Picea pungens* glauca.), and Fountain Grass (*Pennisetum setaceum*). J Geophys Res, 107: 4760

Ji J J, Miao M Q. 1994. Numerical experiments of influence of heterogeneous vegetation distribution on the states of surface and atmospheric boundary layer (in Chinese). Sci Atmos Sin, 18: 293–302

Jiang W M, Miao S G, Zhang N, Liu H N, Hu F, Li L, Wang Y W, Wang C G. 2010. Numerical simulation on urban meteorology and urban boundary layer (in Chinese). Adv Earth Sci, 25: 463–473

Jiang W M, Miao S G. 2004. Large eddy simulation and atmospheric boundary layer—Review and prospect in the past 30 years (in Chinese). Prog Nat Sci, 14: 11–19

Jiménez P A, Dudhia J, González-Rouco J F, Navarro J, Montávez J P, García-Bustamante E. 2012. A revised scheme for the WRF surface layer formulation. Mon Weather Rev, 140: 898–918

Jiménez P A, Dudhia J. 2012. Improving the representation of resolved and unresolved topographic effects on surface wind in the WRF model. J Appl Meteorol Climatol, 51: 300–316

Jiménez P A, Dudhia J, González-Rouco J F, Montávez J P, García-Bustamante E, Navarro J, Vilà-Guerau de Arellano J, Muñoz-Roldán A. 2013. An evaluation of WRF's ability to reproduce the surface wind over complex terrain based on typical circulation patterns. J Geophys Res-Atmos, 118: 7651–7669

Kaimal J C, Finnigan J J. 1994. Atmospheric Boundary Layer Flows: Their Structure and Measurement. New York: Oxford University Press. 289

Kruijt B, Malhi Y, Lloyd J, Norbre A D, Miranda A C, Pereira M G P, Culf A, Grace J. 2000. Turbulence statistics above and within two amazon rain forest canopies. Bound-Layer Meteorol, 94: 297–331

Lalic B, Mihailovic D T. 2004. An empirical relation describing leaf-area density inside the forest for environmental modeling. J Appl Meteorol, 43: 641–645

Launiainen S, Vesala T, MöLder M, Mammarella I, Smolander S, Rannik Ü, Kolari P, Hari P, Lindroth A, G. Katul G. 2007. Vertical variability and effect of stability on turbulence characteristics down to the floor of a pine forest. Tellus B-Chem Phys Meteorol, 59: 919–936

Li H F, Wang B B, Cui G X, Zhang Z S. 2015. Study on thermal environment and pollutant dispersion in real urban area by Large Eddy Simulation (in Chinese). Sci Sin-Phys Mech Astron, 45: 66–82

Li H, Cui G, Zhang Z. 2018. A new scheme for the simulation of microscale flow and dispersion in urban areas by coupling large-eddy simulation with mesoscale models. Bound-Layer Meteorol, 167: 145–170

Liu S H, Deng Y, Hu F, Liang F M, Liu H P, Wang J H. 2004. Numerical simulation of interaction between forest ecosystem and atmosphere boundary layer (in Chinese). Chin J Appl Ecol, 15: 2005–2012

Liu Y J, Miao S G, Hu F, Liu Y B. 2018. Large eddy simulation of flow field over the Xiaohaituo mountain division for the 24th Winter Olympic Games (in Chinese). Plateau Meteorol, 37: 1388–1401

Liu Y S, Cui G X, Wang Z S, Zhang Z S. 2011. Large eddy simulation of wind field and pollutant dispersion in downtown Macao. Atmos Environ, 45: 2849–2859

Liu Y S, Miao S G, Zhang C L, Cui G X, Zhang Z S. 2012. Study on micro-atmospheric environment by coupling large eddy simulation with mesoscale model. J Wind Eng Ind Aerodyn, 107–108: 106–117

Liu Z, Chen J M, Jin G, Qi Y. 2015. Estimating seasonal variations of leaf area index using litterfall collection and optical methods in four mixed evergreen-deciduous forests. Agric For Meteorol, 209–210: 36–48

Lorente-Plazas R, Jiménez P A, Dudhia J, Montávez J P. 2016. Evaluating and improving the impact of the atmospheric stability and orography on surface winds in the WRF model. Mon Weather Rev, 144: 2685–2693

Meneveau C, Lund T S, Cabot W H. 1996. A Lagrangian dynamic subgrid-scale model of turbulence. J Fluid Mech, 319: 353–385

Moeng C H. 1984. A large-eddy-simulation model for the study of planetary boundary-layer turbulence. J Atmos Sci, 41: 2052–2062

Moeng C H, Dudhia J, Klemp J, Sullivan P. 2007. Examining two-way grid nesting for large eddy simulation of the pbl using the WRF model. Mon Weather Rev, 135: 2295–2311

Nakai T, Sumida A, Matsumoto K, Daikoku K, Iida S, Park H, Miyahara M, Kodama Y, Kononov A V, Maximov T C, Yabuki H, Hara T, Ohta T. 2008. Aerodynamic scaling for estimating the mean height of dense canopies. Bound-Layer Meteorol, 128: 423–443

Nebenführ B, Davidson L. 2015. Large-eddy simulation study of thermally stratified canopy flow. Bound-Layer Meteorol, 156: 253–276

Nebenführ B, Davidson L. 2017. Prediction of wind-turbine fatigue loads in forest regions based on turbulent LES inflow fields. Wind Energ, 20: 1003–1015

Pan Y, Chamecki M, Nepf H M. 2016. Estimating the instantaneous drag-wind relationship for a horizontally homogeneous canopy. Bound-Layer Meteorol, 160: 63–82

Pan Y, Follett E, Chamecki M, Nepf H. 2014. Strong and weak, unsteady reconfiguration and its impact on turbulence structure within plant canopies. Phys Fluids, 26: 105102

Parlange M B, Brutsaert W. 1989. Regional roughness of the landes forest and surface shear stress under neutral conditions. Bound-Layer Meteorol, 48: 69–81

Pinard J D J P, Wilson J D. 2001. First- and second-order closure models for wind in a plant canopy. J Appl Meteorol, 40: 1762–1768

Poggi D, Porporato A, Ridolfi L, Albertson J D, Katul G G. 2004. The effect of vegetation density on canopy sub-layer turbulence. Bound-Layer Meteorol, 111: 565–587

Pope S B. 2000. Turbulent Flows. Cambridge: Cambridge University Press. 773

Sauer J A, Muñoz-Esparza D, Canfield J M, Costigan K R, Linn R R, Kim Y J. 2016. A large-eddy simulation study of atmospheric boundary layer influence on stratified flows over terrain. J Atmos Sci, 73: 2615–2632

Schlegel F, Stiller J, Bienert A, Maas H G, Queck R, Bernhofer C. 2012. Large-eddy simulation of inhomogeneous canopy flows using high resolution terrestrial laser scanning Data. Bound-Layer Meteorol, 142: 223–243

Schlegel F, Stiller J, Bienert A, Maas H G, Queck R, Bernhofer C. 2015. Large-eddy simulation study of the effects on flow of a heterogeneous forest at sub-tree resolution. Bound-Layer Meteorol, 154: 27–56

Shaw R H, den Hartog G, Neumann H H. 1988. Influence of foliar density and thermal stability on profiles of reynolds stress and turbulence intensity in a deciduous forest. Bound-Layer Meteorol, 45: 391–409

Shaw R H, Schumann U. 1992. Large-eddy simulation of turbulent flow above and within a forest. Bound-Layer Meteorol, 61: 47–64

Shen S, Leclerc M Y. 1997. Modelling the turbulence structure in the canopy layer. Agric For Meteorol, 87: 3–25

Stoll R, Porté-agel F. 2006. Effect of roughness on surface boundary conditions for large-eddy simulation. Bound-Layer Meteorol, 118: 169–187

Su H B, Schmid H P, Vogel C S, Curtis P S. 2008. Effects of canopy morphology and thermal stability on mean flow and turbulence statistics observed inside a mixed hardwood forest. Agric For Meteorol, 148: 862–882

Tao W Q. 2004. Numerical Heat Transfer (in Chinese). 2nd ed. Xi'an: Xi'an Jiaotong University Press. 537

Tjernström M. 1989. Some tests with a surface energy balance scheme, including a bulk parameterisation for vegetation, in a mesoscale model. Bound-Layer Meteorol, 48: 33–68

Versteeg H K, Malalasekera W. 2007. An Introduction to Computational Fluid Dynamics: The Finite Volume Method. 2nd ed. Harlow: Pearson Prentice Hall. 517

Villani M G, Schmid H P, Su H B, Hutton J L, Vogel C S. 2003. Turbulence statistics measurements in a Northern Hardwood Forest. Bound-Layer Meteorol, 108: 343–364

Vogel S. 1989. Drag and reconfiguration of broad leaves in high winds. J Exp Bot, 40: 941–948

Wang L, Li D, Gao Z, Sun T, Guo X, Bou-Zeid E. 2014. Turbulent transport of momentum and scalars above an urban canopy. Bound-Layer Meteorol, 150: 485–511

Wyngaard J C. 2010. Turbulence in the Atmosphere. New York: Cambridge University Press. 407

Xu L, Pyles R D, Paw U K T, Chen S H, Monier E. 2014. Coupling the high-complexity land surface model ACASA to the mesoscale model WRF. Geosci Model Dev, 7: 2917–2932

Yan C, Huang W X, Miao S G, Cui G X, Zhang Z S. 2017. Large-eddy simulation of flow over a vegetation-like canopy modelled as arrays of bluff-body elements. Bound-Layer Meteorol, 165: 233–249

Yin X Y. 1991. Study on turbulence in vegetation (in Chinese). Adv Mech, 25: 444–456

Yue W, Parlange M B, Meneveau C, Zhu W, van Hout R, Katz J. 2007. Large-eddy simulation of plant canopy flows using plant-scale representation. Bound-Layer Meteorol, 124: 183–203

Zhou X, Beljaars A, Wang Y, Huang B, Lin C, Chen Y, Wu H. 2017. Evaluation of WRF simulations with different selections of subgrid orographic drag over the Tibetan Plateau. J Geophys Res-Atmos, 122: 9759–9772

(Responsible editor: Hongsheng ZHANG)